

**REPORT DOCUMENTATION PAGE**

Form Approved  
OMB No. 0704-0188

The public reporting burden for this collection of information is estimated to average 1 hour per response, including the time for reviewing instructions, searching existing data sources, gathering and maintaining the data needed, and completing and reviewing the collection of information. Send comments regarding this burden estimate or any other aspect of this collection of information, including suggestions for reducing the burden, to the Department of Defense, Executive Service Directorate (0704-0188). Respondents should be aware that notwithstanding any other provision of law, no person shall be subject to any penalty for failing to comply with a collection of information if it does not display a currently valid OMB control number.

**PLEASE DO NOT RETURN YOUR FORM TO THE ABOVE ORGANIZATION.**

<b>1. REPORT DATE (DD-MM-YYYY)</b> 25/02/2010		<b>2. REPORT TYPE</b> Final		<b>3. DATES COVERED (From - To)</b> 15 Dec 06- 30 Nov 09	
<b>4. TITLE AND SUBTITLE</b> MULTISCALE FRACTURE MECHANICS OF 3D REINFORCED COMPOSITES				<b>5a. CONTRACT NUMBER</b> FA9550-07-1-0028	
				<b>5b. GRANT NUMBER</b> FA9550-07-1-0028	
				<b>5c. PROGRAM ELEMENT NUMBER</b>	
<b>6. AUTHOR(S)</b> E.V. Iarve				<b>5d. PROJECT NUMBER</b>	
				<b>5e. TASK NUMBER</b>	
				<b>5f. WORK UNIT NUMBER</b>	
<b>7. PERFORMING ORGANIZATION NAME(S) AND ADDRESS(ES)</b> THE UNIVERSITY OF DAYTON RESEARCH INSTITUTE 300 COLLEGE PARK AVE 8 PERIOD OF PERFORMANCE DAYTON OH 45469-01 04				<b>8. PERFORMING ORGANIZATION REPORT NUMBER</b>	
<b>9. SPONSORING/MONITORING AGENCY NAME(S) AND ADDRESS(ES)</b> Dr. Arje Nachman AF OFFICE OF SCIENTIFIC RESEARCH 875 NORTH RANDOLPH STREET, RM 31 12 ARLINGTON VA 22203				<b>10. SPONSOR/MONITOR'S ACRONYM(S)</b> AFOSR/PKR3	
				<b>11. SPONSOR/MONITOR'S REPORT NUMBER(S)</b> AFRL-SR-AR-TR-10-0094	
<b>12. DISTRIBUTION/AVAILABILITY STATEMENT</b> Public Release A. Unlimited					
<b>20100316240</b>					
<b>13. SUPPLEMENTARY NOTES</b>					
<b>14. ABSTRACT</b> The simply coupled scale analysis method (SCSAM) has been further extended to perform fracture analysis of heterogeneous materials and multilayered composite materials in particular, whereas previously we evaluated strength based on stress levels in undamaged composites. Progressive multicroack fracture simulation on each scale is performed by using the mesh-independent crack propagation technique and cohesive formulation for crack extension. A representative volume element (RVE) approach employed for homogenized stiffness and stress concentration factor computation was extended to compute homogenized cohesive crack opening relationship on the higher hierarchical scale based on the cohesive relationships of the constituents. In the spirit of SCSAM and within the limitation of sufficiently small microstructure scale simulation, the coupling of scales is occurring through hierarchical computation of homogenized properties, which now include fracture properties, whereas the simulation of the failure process on each scale is conducted independently. Such an approach is highly practical and applicable to prediction of complex phenomena in composite and hybrid materials.					
<b>15. SUBJECT TERMS</b>					
<b>16. SECURITY CLASSIFICATION OF:</b>			<b>17. LIMITATION OF ABSTRACT</b> SAR	<b>18. NUMBER OF PAGES</b> 38	<b>19a. NAME OF RESPONSIBLE PERSON</b> Endel V. Iarve
<b>a. REPORT</b> U	<b>b. ABSTRACT</b> U	<b>c. THIS PAGE</b> U			<b>19b. TELEPHONE NUMBER (Include area code)</b> 937 255 9094

**University of Dayton Research Institute**

**Endel V. Iarve**

**MULTI-SCALE FRACTURE MECHANICS OF 3-D REINFORCED  
COMPOSITES**

**Final Report**

**FY07-09**

**Grant Number: FA9550-07-1-0028**

**February 26, 2010**

**Distribution Statement: A. Public Release**

## CONTENT

<b>Summary</b>	<b>3</b>
<b>Personnel, Publications and Awards</b>	<b>4</b>
<b>1. Introduction</b>	<b>5</b>
<b>2. Mesh Independent Intra-Phase and Interface Crack Modeling</b>	<b>6</b>
a. Mesh Independent Crack Modeling	
b. Cohesive Energy and Interface Crack Modeling	
c. Variational Formulation and Problem Solution	
<b>3. Intra-Phase (Ply) MIC and Interface Cracking (Delamination) Interaction Verification Study</b>	<b>13</b>
a. Transverse Crack Tension Test (TCT)	
<b>4. Effective Fracture Toughness Computation</b>	<b>16</b>
a. Cubic Unit Cell	
b. Hexagonal Unit Cell	
c. Application to Thermal Oxidation	
d. Future Directions	
<b>5. Complex Interactive Cracking Network Simulation on the Ply Level</b>	<b>28</b>
<b>Appendix: Composite Scarf Repair Optimization for the JSF</b>	<b>33</b>
<b>References</b>	<b>36</b>

## Summary:

The simply coupled scale analysis method (SCSAM) has been further extended to perform fracture analysis of heterogeneous materials and multilayered composite materials in particular. This work is based on Breitzman, et al. [1] and Lipton [2,3] SCSAM work allowing prediction of the local stress and strain fields inside undamaged pre-stressed composites. SCSAM allowed for rigorous micro-level stress bound evaluation in the presence of stress gradients, including regions where periodicity is not maintained in all directions. This methodology allowed evaluating the strength of composite scarf repair and optimizing the repair patch stacking sequence to design repair satisfying low observability requirements. Although basic results on repair analysis were reported in the previous FY04-06 period, the results of the optimization study were obtained later and are included in the present report. Critical development of the present project is an extension of SCSAM to simulate the failure process, whereas previously we evaluated strength based on stress levels in undamaged composites. Progressive multi-crack fracture simulation on each scale is performed by using the mesh-independent crack propagation technique and cohesive formulation for crack extension. A representative volume element (RVE) approach employed for homogenized stiffness and stress concentration factor computation was extended to compute homogenized cohesive crack opening relationship on the higher hierarchical scale based on the cohesive relationships of the constituents. In the spirit of SCSAM and within the limitation of sufficiently small microstructure scale simulation, the coupling of scales is occurring through hierarchical computation of homogenized properties, which now include fracture properties, whereas the simulation of the failure process on each scale is conducted independently. Such an approach is highly practical and applicable to prediction of complex phenomena in composite and hybrid materials. An example of application of this methodology is simulation of thermo-oxidative cracking in high-temperature composites, which we conducted recently in support of the Hybrids for Extreme Environments Program in AFRL/RXBC; Marilyn Unroe is the program manager, e-mail: [Marilyn.Unroe@wpafb.af.mil](mailto:Marilyn.Unroe@wpafb.af.mil) and Dr. Vernon Beehel technical lead, e-mail: [Vernon.Beehel@wpafb.af.mil](mailto:Vernon.Beehel@wpafb.af.mil). We have also performed simulations of complex failure patterns in multilayered composites under more traditional loading in ambient conditions.

Further research is required to address the anisotropy of the fracture toughness in materials with strongly anisotropic homogenized properties and related questions of the influence of the RVE on the results of the homogenized cohesive relationship prediction. A critical underlying technology for application and development of progressive fracture modeling, SCSAM is a technique for modeling complex multiple site initiation and crack propagation patterns in three-dimensional formulation, which also requires further development. It is also envisioned that the future development path of the SCSAM framework should include nonclassical crack models at a small length scale.

### **Personnel and Collaborators:**

Principal Investigator- Dr. Endel V. Iarve, UDRI

Co-Principal Investigator- Prof. Robert Lipton, LSU (no direct charge to the grant)

Dr. Timothy Breitzman, AFRL (no direct charge to the grant)

### **Journal Publications:**

Breitzman, T., Iarve, E., Cook, B, and Schoeppner, G, and Lipton, R. "Optimization of a composite scarf repair patch under tensile loading." *Composites Part A: Applied Science and Manufacturing*, 40, 2009, pp.1921-1930.

### **Conference Presentations/Proceedings:**

T. Breitzman, E. Iarve, D. Mollenhauer, G. Schoeppner, B. Cook, "Tensile failure prediction and measurement in composite scarf repair," Invitation-only, special symposium on damage mechanics at the 13th European Conference on Composite Materials, Stockholm, Sweden, 2-5 June 2008.

T. Breitzman, E. Iarve, E. Ripberger, "Optimal design of a composite scarf repair under uniaxial tension loading," 2009 ASME IMECE, Lake Buena Vista, FL, 13-19 Nov 2009.

T. Breitzman, E. Iarve, R. Lipton, B. Cook, "Optimal design of a composite scarf repair under uniaxial tension loading," 17th International Conference on Composite Materials, Edinburgh, UK, 27-31 Jul 2009.

T. Breitzman, E. Iarve, G. Schoeppner, B. Cook, "Optimal design of a composite scarf repair under uniaxial tension loading," 2009 SAMPE, Baltimore, MD, 18-21 May 2009.

T. Breitzman, E. Iarve, D. Mollenhauer, E. Zhou, T. Whitney, "Detailed morphology modeling and residual stress evaluation in tri-axial braided composites," 50th American Institute of Avionics and Aeronautics Conference on Structures, Dynamics, and Materials, Palm Springs, CA, 4-7 May 2009.

T. Breitzman, E. Iarve, G. Schoeppner, G. Cook, "Optimal design of a composite scarf repair under uniaxial tension loading," 2008 ASME IMECE, Boston, MA, 2-6 Nov 2008.

T. Breitzman, E. Iarve, G. Schoeppner, B. Cook, "Optimal design of a composite scarf repair patch under uniaxial tension load," 4th International Conference on Composites Testing and Model Identification, Dayton, OH, 20-22 Oct 2008.

T. Breitzman, E. Iarve, D. Mollenhauer, G. Schoeppner, B. Cook, "Tensile failure prediction and measurement in composite scarf repair," 2007 ASME IMECE, Seattle, WA, 5-10 Nov 2007.

T. Breitzman, R. Lipton, E. Iarve, "Local field assessment inside multi-scale composite microstructures," 6th International Congress on Industrial and Applied Mathematics, Zurich, Switzerland, 16-20 Jul 2007.

## Awards

T. Breitzman, Materials & Manufacturing Directorate 2009 Robert T. Schwartz Award for Engineering Achievement

E. Iarvc, Wohlleben/Hochwalt Outstanding Professional Research Award, University of Dayton, 2008

## 1. Introduction and State of the Art

To date, the primary approach used for multi-scale failure prediction in composite material is the so-called continuum damage mechanics (CDM) method [4-6]. According to this method the effect of damage at each length scale is manifested by local stiffness degradation at the higher (coarser) length scale. The attractiveness of this technique is in the intuitiveness of its concept and the ease of implementation. One reason for the popularity of CDM is the potential ability to model an arbitrary path of damage propagation on the macro-scale using numerical schemes based upon a standard finite element (FE) formulation. The drawback of these models is their inability to accurately describe the local effects of interaction of various damage modes and local effects of stress redistribution in the damaged area as discussed by Iarve, et al. [7]. Instead, a computational framework based on discrete modeling of arbitrary multiple interacting cracking is chosen for development and implementation of SCSAM.

Several methodologies have been proposed for modeling the kinematics of arbitrary cracking. Evolution of a crack front can be captured by traditional FE modeling combined with adaptive remeshing techniques [8]. Successful in predicting complex crack evolution in metallic structures, its application to predicting crack scenarios in laminated composites, where cracks form in different plies in adjacent locations, will require remeshing of significant volumes under multiple mesh compatibility constraints. An alternative approach to modeling crack-induced displacement discontinuities involves mesh independent crack modeling techniques. Early works devoted to mesh independent modeling of matrix cracking in composite laminates include [9, 10]. Over the last decade, following the pioneering work of Moës, et al. [11] in which the concept of the eXtended Finite Element Method (x-FEM) was proposed, a significant effort to further develop these ideas has been put forth. Although most of the research was devoted to arbitrary crack propagation in isotropic materials, recent application to composite materials includes delamination modeling and textile composite architecture representation [12, 13].

In the present development we target complex materials where several hierarchical scales exist. Two types of cracking need to be generally recognized in such systems: the interface cracking and arbitrary three-dimensional intra-phase cracking, as shown in Figure 1. This classification is applicable on each hierarchical scale, i.e. Figure 1 shows a schematic view of a multilayered composite skin. Figure 1.b shows both interface and intra-phase (ply) cracking on the ply scale level. Interface and intra-phase

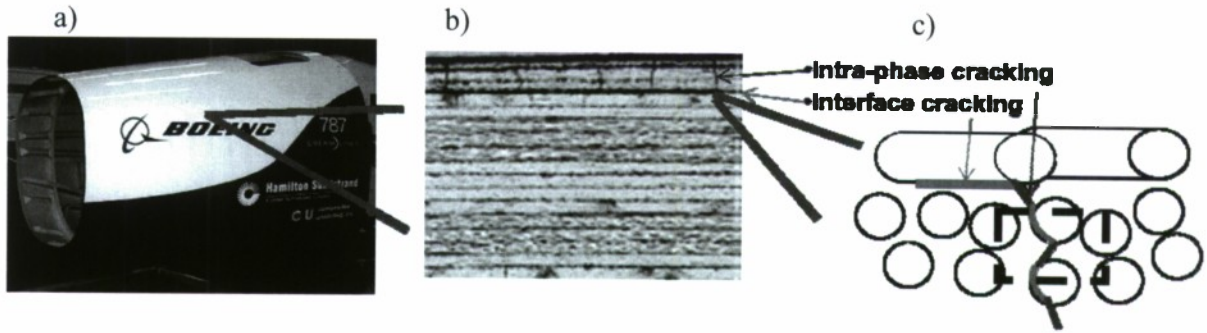


Figure 1. Hierarchical composite structure

matrix cracking on the fiber matrix level is shown in Figure 1.c. In this case the interface cracking is between the matrix and the individual fibers, and the intra-phase cracking is inside the matrix. In order to facilitate the SCSAM, a computational framework capable of originating and evolving complex interface and intra-phase cracking networks without any prior knowledge or assumptions regarding the locations of damage origination is required.

Our analysis is built around a regularized x-FEM formulation (Iarve [14]), which is extended to multiple crack initiation and evolution modeling. In a regularized formulation, the step function describing the crack surface is replaced by a continuous function and consequently allows one to maintain a Gauss integration schema for element stiffness matrix computation without regard to crack orientation. In this case the connection between two arbitrarily cracked surfaces can be easily established by computing integrals of the products of the shape functions on the two surfaces.

We begin by outlining the regularized mesh independent crack (MIC) modeling framework, followed by the nonlinear homogenization of the RVE containing evolving cracks. Next we will discuss computation of the homogenized effective stiffness and strength and fracture toughness properties of high-temperature unidirectional G3-500/PMR15 composites subjected to thermal oxidation. Finally, we illustrate complex fracture phenomena in a laminated composite such as is shown in Figure 1.

## 2. Mesh Independent Intra-Phase and Interface Crack Modeling

As mentioned before we seek a framework capable of accommodating the initiation and interactive evolution of both intra-phase and interface cracking. Without restricting the generality, we shall consider a laminated media, where the interface cracks represent delamination and the intra-phase cracks are transverse cracks. An application to arbitrary surface geometry, where the interface cracks will represent fiber surfaces, will be considered in the next section.

### a. Mesh Independent Crack Modeling

Consider a partition of unity set of continuous basis functions  $X_i(\mathbf{x})$  and a displacement approximation on the domain of interest  $V$ .

$$\mathbf{u}(\mathbf{x}) = \sum_{i \in \Omega} X_i(\mathbf{x}) \mathbf{U}_i \quad (1)$$

Next consider a crack appearing in this volume, as shown in Figure 2, with a surface  $\Gamma_\alpha$  defined, by means of the signed distance function defined as:

$$f_\alpha(\mathbf{x}) = \text{sign}(\mathbf{n}(\bar{\mathbf{x}})(\mathbf{x} - \bar{\mathbf{x}})) \min_{\bar{\mathbf{x}} \in \Gamma_\alpha} \|\mathbf{x} - \bar{\mathbf{x}}\| \quad (2)$$

where  $\mathbf{n}(\bar{\mathbf{x}})$  is the normal to the crack surface  $f_\alpha$  at the point  $\bar{\mathbf{x}}$ . The traditional x-FEM strong discontinuity formulation is based on the element enrichment with displacement modes discontinuous over the crack surface by introducing shape functions multiplied by  $H(f_\alpha(\mathbf{x}))$ , where  $H(x)$  is the Heaviside step function. Consider a partition of unity set of continuous basis functions  $X_i(\mathbf{x})$  and a displacement approximation on the domain of interest  $V$ .

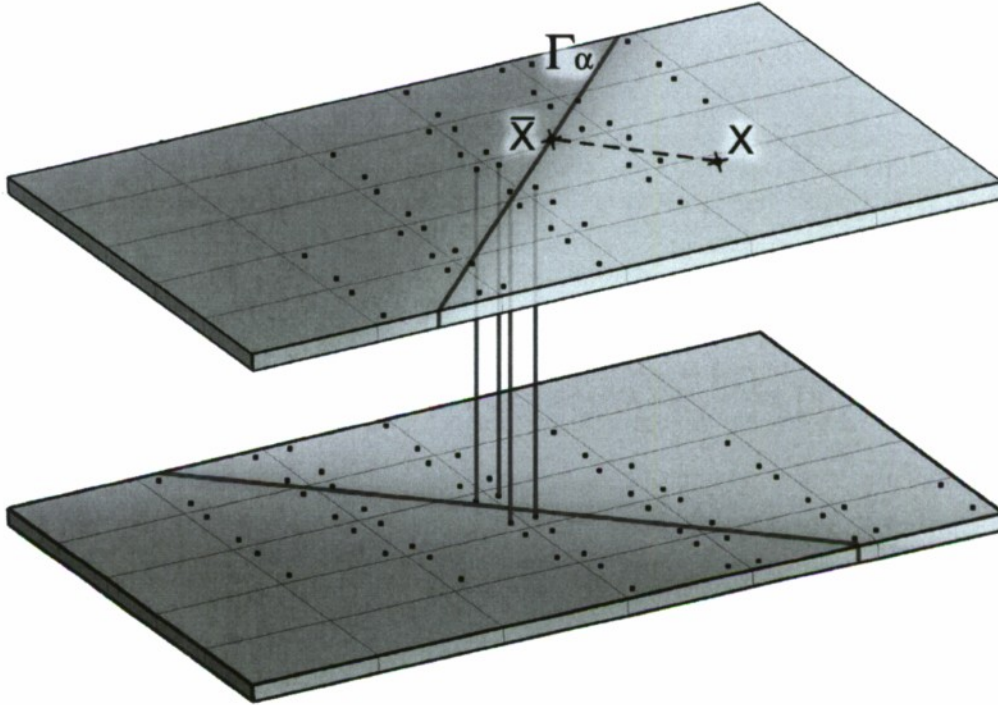


Figure 2. Signed distance function for arbitrary matrix crack definition and schematics of cross integral computation for adjacent ply interfaces in the regularized formulation.

In the regularized formulation [14] the Heaviside step function is replaced with a continuous function  $\tilde{H}(\mathbf{x})$

$$\tilde{H}(\mathbf{x}) = \sum_{i \in \Omega} X_i(\mathbf{x}) h_i \quad (3)$$

where  $X_i(\mathbf{x})$  are the same shape functions as in Eqn. (1). The coefficients  $h_i$  are calculated as follows

$$h_i = \frac{1}{2} \left( 1 + \frac{\int_V f_\alpha(\mathbf{x}) X_i(\mathbf{x}) d\mathbf{x}}{\int_V |f_\alpha(\mathbf{x})| X_i(\mathbf{x}) d\mathbf{x}} \right). \quad (4)$$

This definition involves only continuous functions and can be calculated by using standard Gauss quadratures. The only coefficients  $h_i$ , which are not equal to 0 or 1, correspond to those shape functions that are divided by the crack surface. Let us denote the set of such index values (for which  $h_i$  is not equal to 0 or 1) by  $\Omega_\alpha$ . Then the enriched approximation for the domain  $V$  and arbitrary crack is defined in the following form

$$\mathbf{u} = \tilde{H} \mathbf{u}^{(1)} + (1 - \tilde{H}) \mathbf{u}^{(2)} + \mathbf{u}^{(3)} \quad (5)$$

$$\mathbf{u}^{(1)} = \sum_{i \in \Omega_\alpha} X_i \mathbf{U}_i^{(1)}, \quad \mathbf{u}^{(2)} = \sum_{i \in \Omega_\alpha} X_i \mathbf{U}_i^{(2)}, \quad (6)$$

and

$$\mathbf{u}^{(3)} = \sum_{i \in \Omega / \Omega_\alpha} X_i \mathbf{U}_i^{(3)} \quad (7)$$

We have also omitted the spatial argument for conciseness. The displacement approximation given in Eqn. (9) contains the enrichment in the crack region via displacement fields  $\mathbf{u}^{(1)}$  and  $\mathbf{u}^{(2)}$  as well as the unchanged displacement field,  $\mathbf{u}^{(3)}$  away from the crack. Equations (5)-(7) define the enriched displacement approximation by replacing each original shape function  $X_i$  influenced by the crack,  $i \in \Omega_\alpha$ , with two shape functions,  $\tilde{H} X_i$  and  $(1 - \tilde{H}) X_i$ . This approximation was applied in [14] in conjunction with a higher order  $C^0$  displacement approximation (p-elements) as well as B-spline approximation of displacements, where the coefficients  $\mathbf{U}_i$  do not correspond to nodal displacements. The convenience of such representation of the enrichment lies in the simplicity of bookkeeping the connectivity, where the two copies of the shape function do not interact and are connected with only alike  $\tilde{H}$  or  $(1 - \tilde{H})$  multiple copies of the other enriched shape function if their supports overlap.

The strain energy in the volume  $V$  with displacement approximation given in Eqn. (5) is written as

$$\begin{aligned}
W = \int_V \{ & \tilde{H}(\boldsymbol{\varepsilon}^{(1)} - \mathbf{e})^T \mathbf{C}(\boldsymbol{\varepsilon}^{(1)} - \mathbf{e}) + (1 - \tilde{H})(\boldsymbol{\varepsilon}^{(2)} - \mathbf{e})^T \mathbf{C}(\boldsymbol{\varepsilon}^{(2)} - \mathbf{e}) \\
& + (\boldsymbol{\varepsilon}^{(3)} - \mathbf{e})^T \mathbf{C}(\boldsymbol{\varepsilon}^{(3)} - \mathbf{e}) + \tilde{H}(\boldsymbol{\varepsilon}^{(1)} - \mathbf{e})^T \mathbf{C}(\boldsymbol{\varepsilon}^{(3)} - \mathbf{e}) \\
& + (1 - \tilde{H})(\boldsymbol{\varepsilon}^{(2)} - \mathbf{e})^T \mathbf{C}(\boldsymbol{\varepsilon}^{(3)} - \mathbf{e}) \} dV
\end{aligned} \quad (8)$$

where superscript T means transpose operation,  $\mathbf{C}$  is the elastic orthotropic stiffness tensor, and  $\mathbf{e}$  is the nonmechanical strain tensor introduced to account for thermal processing stresses, so that  $\mathbf{e} = (T - T_0)\boldsymbol{\alpha}$ . Here  $T$  and  $T_0$  are cure and ambient temperature, and  $\boldsymbol{\alpha}$  is the thermal expansion tensor. The components of the stiffness tensor in the arbitrary coordinate system can be expressed according to [15]. The strain tensors  $\boldsymbol{\varepsilon}^{(k)}$  are computed from displacement fields  $\mathbf{u}^{(k)}$  in Eqn. (5), so that

$$\boldsymbol{\varepsilon}^{(k)} = \frac{1}{2}(\nabla \mathbf{u}^{(k)} + \mathbf{u}^{(k)} \nabla). \quad (9)$$

Expression (9) does not contain the interaction energy in the gradient zone, which will be considered next. Typically, in a regularized formulation, the MIC propagation is governed by the constitutive properties in the gradient zone, in which  $|\nabla \tilde{H}| = \sqrt{\nabla \tilde{H} \cdot \nabla \tilde{H}} > 0$ . In the present formulation, the cohesive constitutive relationship [16] developed for interface fracture modeling is inserted into the gradient zone of the regularized formulation directly. It can be accomplished by using Dirac's delta function of signed distance function of the crack surface to express the cohesive energy of the crack surface through the volume integral in the gradient zone. Indeed the surface  $S_v$  with signed distance function  $f_\alpha$  enclosed in an arbitrary volume  $v$  can be expressed as a volume integral

$$S_v = \int_v \delta_D(f_\alpha) dV \quad (10)$$

where  $\delta_D(f_\alpha)$  is the Dirac's delta function of signed distance function. One can also establish that for an arbitrary continuous function  $g(\mathbf{x})$  defined in volume  $V$ , a relationship between the surface integral over the crack surface  $\Gamma_\alpha$  ( $\Gamma_\alpha \subset V$ ) and a volume integral exists so that

$$\iint_{\Gamma_\alpha} g(\mathbf{x}) dS = \int_V g(\mathbf{x}) \delta_D(f_\alpha) dV \quad (11)$$

This relationship can be readily established by applying Eqn. ( 10) in small adjoining volumes encompassing surface  $\Gamma_\alpha$  to develop the integral sums representing the left- and right-hand side of Eqn. ( 11). In the case of the regularized formulation we compute the approximate value of the right-hand side by replacing the Dirac's function  $\delta_D(f_\alpha)$  by the gradient of the approximate step function  $|\nabla\tilde{H}|$ . The continuous function  $g(\mathbf{x})$  defined over the volume is now replaced with the point wise cohesive energy of crack opening. In the traditional interface cohesive formulation, the cohesive energy is a function of the crack opening displacement and is also dependent on the ratio of the opening mode I (perpendicular to crack surface) and the shearing mode II tangential to the crack surface. To separate these modes one needs to know the direction of the normal to the crack surface in all points. In the regularized formulation, the displacement gap and the normal vector are defined in all points of the gradient zone as

$$\Delta\mathbf{u}=\mathbf{u}^{(1)} - \mathbf{u}^{(2)} \text{ and } \mathbf{n} = \nabla f_\alpha \quad (12)$$

where  $\mathbf{u}^{(1)}$  and  $\mathbf{u}^{(2)}$  are defined by using the displacement fields in enriched approximation ( 5). The cohesive energy of the crack opening  $g(\mathbf{x})$  will be considered homogeneous and therefore dependent upon the spatial coordinate  $\mathbf{x}$  only as a function of the displacement gap and the normal vector to the crack surface, so that  $g(\mathbf{x})=g(\Delta\mathbf{u}, \mathbf{n})$ . Thus the fracture energy of the MIC propagation is expressed as

$$M = \int_V |\nabla\tilde{H}| g(\Delta\mathbf{u}, \mathbf{n}) dV. \quad (13)$$

### b. Cohesive Energy and Interface Crack Modeling

The shape of the interface cohesive energy function in composite laminates for predicting the delamination failure mode has been studied extensively including [16-18]. It can be written down in the invariant form a function of the absolute value of the displacement gap  $\lambda=|\Delta\mathbf{u}|$  and a mode mixity parameter, such as

$$B = 1 - \frac{(|\Delta u_n| + \Delta u_n)^2}{4\lambda^2},$$

introduced in [16], where  $\Delta u_n = (\Delta\mathbf{u} \cdot \mathbf{n})$  is the normal component of the displacement gap, which is equal to 0 for mode I propagation and 1 for mode II propagation. The shape of the relationship  $g(\lambda, B)$  can vary; however, to assure the correct crack propagation characteristics, it must satisfy the following condition

$$g(\infty, B) = G_c(B), \quad (14)$$

$$G_c(B) = G_{Ic} + (G_{Ic} - G_{IIc})B^\eta,$$

where  $G_{Ic}$  and  $G_{IIc}$  are experimentally measured fracture toughness values and  $\eta=2.25$ . The functional shape of the fracture energy as a function of the displacement gap is defined by the relationship between the cohesive tractions and the displacement gap, which in [16] is assumed:

$$\boldsymbol{\tau} = (1 - d)K\Delta\mathbf{u} + dK\langle\Delta\mathbf{u} \cdot \mathbf{n}\rangle, \quad (15)$$

where  $K$  is high initial stiffness and  $d$  is the damage parameter. The first term in Eqn. (15) represents the crack cohesive force, and the second term prevents interpenetration. The brackets  $\langle x \rangle = \frac{1}{2}(x + |x|)$  represent the McAuley operator. A bilinear relationship is assumed for  $\tau(\lambda)$  such that  $d=0$  if  $\lambda < \Delta_0$  and  $d=1$  if  $\lambda > \Delta_f$ . The cohesive energy  $g(\lambda, B)$  is the area under the  $\tau(\lambda)$  curve, and thereby according to Eqn. (14), the final value of the displacement gap is determined by its initial value and the fracture toughness as

$$\Delta_f = 2G_c / (K\Delta_0)$$

The initial value of the displacement gap, beyond which the interface failure begins, is defined as

$$\Delta_0 = \tau_0 / K,$$

where  $\tau_0$  is the initial strength, also depending on the mode mixity parameter  $B$  as follows

$$(\tau_0)^2 = Y^2 + (S^2 - Y^2)B^\eta$$

where  $Y$  and  $S$  are the transverse and shear strengths, respectively. All parameters entering the analysis, such as the fracture toughness and strength values, represent material properties and are measured by using standard test methods. The reader is referred to reference [16] for full details, and the brief description above is given for completeness of the present formulation.

The cohesive energy associated with the delamination of the plies is computed by integrating the cohesive energy over the interface between plies  $n$  and  $n+1$ , separated by the horizontal surface  $z=z_n$  is

$$\Phi_n = \iint_{z=z_n} g(\lambda, B) ds \quad (16)$$

In this case the normal vector to the crack surface is  $(0,0,1)$ , and the displacement gap between the interfaces is computed by using enriched displacement approximations (5) in all plies.

### c. Variational Formulation and Problem Solution

The work of the external traction  $\mathbf{P}$  applied at the portion  $S_p$  of the boundary  $\partial V$  is expressed as

$$A = \int_{S_p} \mathbf{P} \mathbf{u} dS \quad (17)$$

To derive the equilibrium equations in terms of the displacement approximation coefficients for a body which contains multiple matrix and delamination cracks, the first variation of the potential energy is required to vanish. Combining Eqs. ( 8), ( 13), ( 16) and ( 17) for the volume strain energy and the work of the surface tractions, and summing over all plies and interfaces, gives,

$$\delta(\sum_{n=1}^N (W_n + M_n) + \sum_{n=1}^{N-1} \Phi_n - A) = 0 \quad (18)$$

The lower indexes in strain energy  $W_n$  and the MIC cohesive energy  $M_n$  designate that they are computed for the  $n$ -th ply; the delamination free energy  $\Phi_n$  is between the  $n$  and  $n+1$ -th ply. Performing the variation, the following system of equations is obtained

$$(\mathbf{W} + \mathbf{M} + \mathbf{\Phi}) \mathbf{U} = \mathbf{P} + \mathbf{N}. \quad (19)$$

The vector of unknowns is arranged by ply in the order  $\mathbf{U}^T = (\mathbf{U}^{(1)}, \mathbf{U}^{(2)}, \mathbf{U}^{(3)}, \dots)^T$ . The matrix  $\mathbf{W}$  and right-hand-side vector  $\mathbf{N}$  are obtained from a variation of  $W_n$  and are the elastic stiffness matrix and the nonmechanical load vector, where the shape functions and/or their derivatives in each integration point are multiplied by  $\tilde{H}$  or by  $(1 - \tilde{H})$ , or unmodified.

In the case when MICs are present in adjacent plies, i.e.  $n$  and  $n+1$ , the displacements  $\mathbf{u}_n$  and  $\mathbf{u}_{n+1}$  are enriched according to Eqn. ( 5). When regularized enrichment is used, the integration of all shape functions is conducted on the original Gauss points, and thereby is straightforward for arbitrary enrichment of displacements in the adjacent plies. Two sparse matrices  $\mathbf{F}_n^n$  and  $\mathbf{F}_n^{n+1}$  are formed at the interface between plies  $n$  and  $n+1$ . For each integration point (always common for plies  $n$  and  $n+1$ ) on the common interface (row index), these matrices contain the values of all nonzero shape functions in this point (column index) for the ply  $n$  and ply  $n+1$ , respectively. These matrices have large dimensions but are very sparse. Matrix  $\mathbf{\Phi}$  can then be represented in the following form

$$\mathbf{\Phi} = \sum_{n=1}^{N-1} (\mathbf{F}_n^{n+1} - \mathbf{F}_n^n)^T \mathbf{D} (\mathbf{F}_n^{n+1} - \mathbf{F}_n^n) \quad (20)$$

The weight matrix  $\mathbf{D}$  is a diagonal matrix containing the Gauss weights and surface Jacobian at the given integration point multiplied by the cohesive stiffness  $(1-d)K$ . Note that the matrices  $\mathbf{F}_n$  can also be used to compute the displacement gap  $\Delta \mathbf{u}$  in each integration point by simple multiplication  $(\mathbf{F}_n^{n+1} - \mathbf{F}_n^n)\mathbf{U}$ . By knowing the displacement gap, one can update the damage variable and the coefficients of decohesive stiffness in each integration point.

The matrix  $\mathbf{M}$  has a structure similar to  $\Phi$ . For opening of the MICs, the matrices of shape function values in integration points are formed so that  $\mathbf{F}_n^1$  and  $\mathbf{F}_n^2$  contain the functions corresponding to enrichments  $\mathbf{u}^{(1)}$  and  $\mathbf{u}^{(2)}$  in Eqn. ( 5), respectively, and the components of the weight matrix, which we denote  $\tilde{\mathbf{D}}$  to distinguish from the delamination case  $\mathbf{D}$ , are the products of Gauss weight, Jacobian,  $|\nabla \tilde{H}|$  and the decohesive stiffness  $(1-d)K$  in the given integration point. Thus the contribution of variation of the MIC opening energy can be written as

$$\mathbf{M} = \sum_{n=1}^N (\mathbf{F}_n^1 - \mathbf{F}_n^2)^T \tilde{\mathbf{D}} (\mathbf{F}_n^1 - \mathbf{F}_n^2). \quad (21)$$

The loading vector  $\mathbf{P}$  comprises of applied external stress as well as displacement loading. Let the vector of displacement approximation coefficients at the edges  $x=0, L$  of the thermal expansion problem with the boundary conditions be  $\mathbf{Q}_0$ . Then the load vector at the load step  $k$  is

$$\mathbf{P} = \mathbf{Q}_0 + \mathbf{Q}_1 \sum_{i=1}^k \Delta_i$$

where  $\mathbf{Q}_i$  is a vector of unit vector displacement at  $x=0, L$  and  $\Delta_i$ - are load increments at the  $i$ -th step.

The system of equations ( 21) contains highly nonlinear components  $\mathbf{M}$  and  $\Phi$  and is solved by using the Newton-Raphson (NR) method at each step.

### 3. Intra-Phase (Ply) Mic and Interface Cracking (Delamination) Interaction Verification Study

Numerical results devoted to verification and application of the proposed methodology for failure prediction in laminated composites will be presented below. The verification will consist of modeling failure in specimens with predefined matrix cracking patterns and comparison with experimental data and FE analysis. The purpose of the following example is to test the methodology of interface and intra-phase cracking, represented by MIC. In this case we are less concerned with hierarchical reproduction of the orthotropic unidirectional composite ply properties entering this analysis. However, it is pertinent to discuss the set of material properties required for a ply level fracture simulation in a composite laminate. These properties pertain to a unidirectional ply and are listed for the material system T300/914C in Table 1. We have divided these properties in two groups. The first group represents stiffness and thermal expansion characteristics, which can be readily computed by using methodology given by Breitzman, et al. [1] from the fiber matrix level constituent. It is the second group of

properties, homogenization of which we will be discussing in the next section. At present we will use the values given in Table 1 obtained experimentally.

Table 1. Material properties used for validation and strength prediction examples

Comments	Property	T300/914C Ref. [20]	IM7/8552 Ref. [32]
<i>Group I : Stiffness and Thermal Expansion Properties</i>	$E_{11}$ (GPa)	139.9	161
	$E_{22}, E_{33}$ (GPa)	10.1	11.38
	$G_{23}$ (GPa)	3.7	3.98
	$G_{12,13}$ (GPa)	4.6	5.17
	$\nu_{23}$	0.436	0.436
	$\nu_{12}, \nu_{13}$	0.3	0.32
	$\alpha_{11}$ ( $1/^\circ\text{C}$ )	$0.4 \times 10^{-6}$	0
	$\alpha_{22}, \alpha_{33}$ ( $1/^\circ\text{C}$ )	$2.5 \times 10^{-5}$	$3 \times 10^{-5}$
<i>Processing</i>	$T-T_0$ ( $^\circ\text{C}$ )	-150	-150
<i>Group II: Strength and Fracture Toughness</i>	$Y_t$ (MPa)	80	60
	$Y_c$ (MPa)	300	260
	$S$ (MPa)	100	90
	$G_{IC}$ ( $\text{J}/\text{M}^2$ )	120	200
	$G_{IIC}$ ( $\text{J}/\text{M}^2$ )	500	1000

#### a. Transverse Crack Tension Test (TCT)

The TCT specimen described in reference [20] was examined to evaluate the accuracy of delamination propagation prediction, which emanates from a MIC. This specimen consists of three unidirectional plies with thickness  $t$ ,  $2t$  and  $t$ , respectively, and is subjected to axial tension. The middle ply is cut at the center through the width. When the tensile loading is applied at the  $x=0, L$  edges in the  $x$ -direction, the applied stress at

first increases linearly until the crack in the middle ply will initiate delaminations between the middle and the outer plies. These delaminations will then propagate in a stable manner keeping the applied stress constant. Finally after the delaminations reach the grips, the load will start increasing again but with a different slope. This configuration allows one to examine the effect of delamination origination from a single matrix crack and was chosen for model validation purposes. The problem was solved both by using the standard FE model, shown in Figure 3a, and the MIC model, shown in Figure 3b. In both cases, cohesive interfaces were implemented on the surfaces between plies. Only half the laminate was modeled, i.e. two plies with equal thickness  $t$  and zero  $z$ -displacement condition on the surface  $z=0$ . In the case of the FE model, the crack in the middle ply is aligned with a mesh line and simply modeled by using double nodes. No mesh line aligned with the initial crack exists in the case of curved nonuniform mesh in Figure 3b, and the MIC model is used to insert the crack in the middle ply only. The sign distance function is  $f_a=x-L/2$ . The total number of axial intervals in the two models coincides; however, due to mesh nonuniformity, the local density of the MIC mesh varies significantly. Applied displacement versus applied load, predicted by the two models, is shown in Figure 4 and are nearly identical.

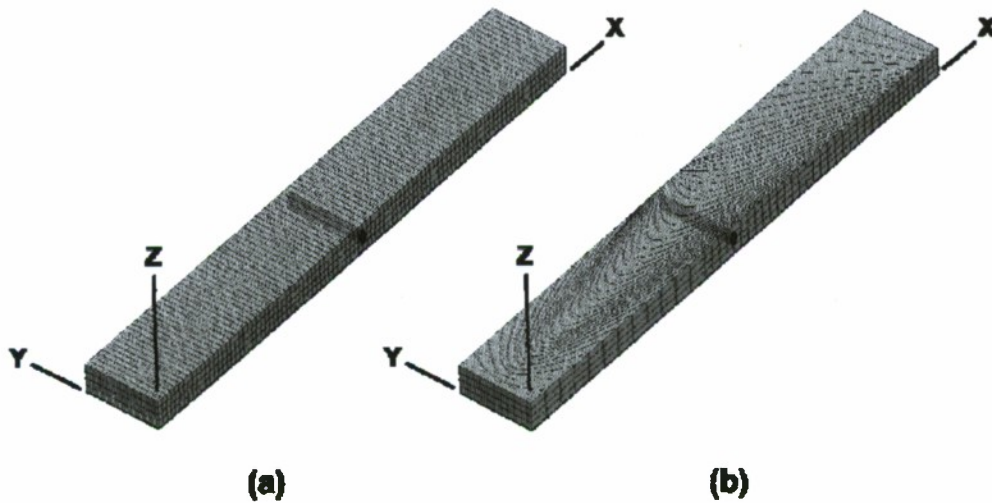


Figure 3. Transverse crack tension (TCT) specimen. Conventional model (a) and MIC evaluation model with skewed mesh.

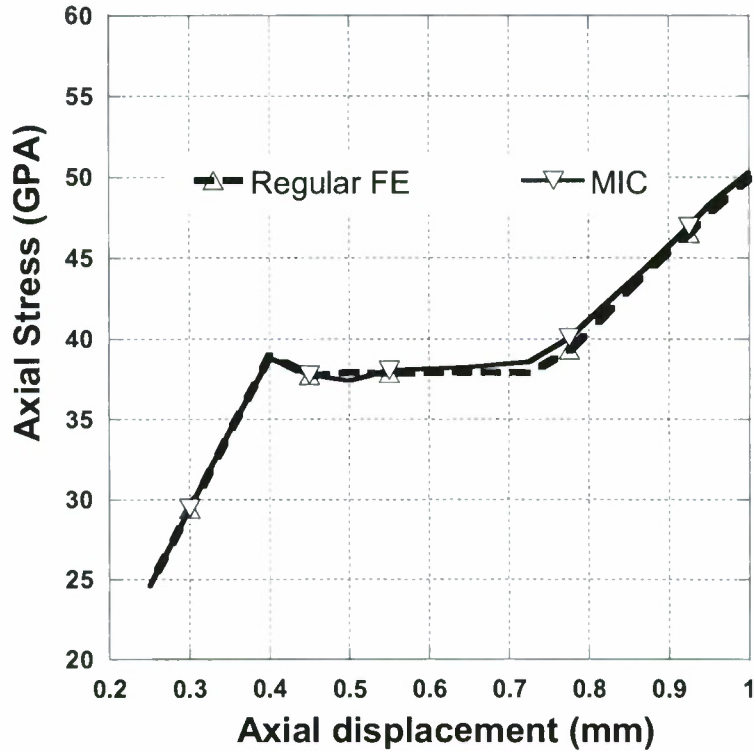


Figure 4. Load displacement curves of the TCT specimen testing predicted by using conventional FE model and MIC.

#### 4. Effective Fracture Toughness Computation

Fracture toughness of composite materials is a strongly anisotropic characteristic. References [21, 22] capture the development of fracture toughness measurement standards and the physics of mixed-mode delamination in unidirectional composites. Very little work has been performed on experimental investigation of the relationship between fracture toughness of the matrix and fiber matrix interfaces and that of the effective fracture toughness of the composite [23,24]. Below we attempt to predict these characteristics. We first describe the simplest RVE, which is capable of representing the stiffness portion of the composite properties, i.e. the Cubic Unit Cell, and on its example, the fracture toughness homogenization methodology. As will be shown, the minimum requirements to an RVE for fracture toughness characterization are not satisfied for this configuration, and next we consider the Hexagonal Unit Cell. We end with the application of the developed methodology to Thermal Oxidation, and Future Directions. Only Mode-I fracture toughness of a unidirectional composite has been addressed at present.

The Mode I fracture toughness ( $G_{Ic}$ ) of a composite is experimentally determined from the double cantilever beam (DCB) test schematically shown in Figure 5. At a

critical tensile load applied to the ligaments, a pre-existing crack is starting to advance. This load is recorded and used to evaluate the fracture toughness at the crack tip at the propagation onset. The fracture toughness determined from this experiment is defined as the Mode I fracture toughness of the composite.

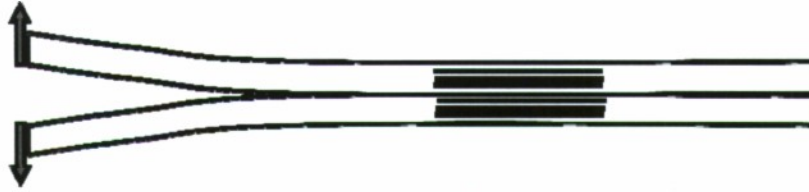


Figure 5. DCB test schematic for Mode I fracture toughness.

The purpose of this work is to understand how to predict Mode I fracture toughness at the ply length scale from simulations at the fiber/matrix microstructural length scale.

#### a. Cubic Unit Cell

Perhaps the simplest unit cell used to represent a fiber-reinforced composite is the cubic unit cell. A two-fiber model (see Figure 6) is used to predict ply-level Mode I fracture toughness for the composite. The dimensions of the two-fiber model are  $L \times L \times 2L$  ( $x \times y \times z$ ), with the origin of the coordinate system as shown in Figure 6. For illustrative purposes, red arrows have been added to show the location of the cohesive zone interface. The cohesive zone is the fracture surface for this model. The cohesive zone interface model is defined across an interface as a combination of normal displacement, total displacement, surface tractions, and fracture toughness as previously described. For all simulations in this section, a 60% fiber volume fraction is assumed unless otherwise noted. Input stiffness and thermal expansion properties for the fiber and matrix phases are summarized in Table 2 and are from reference [24]. We also show the Group I stiffness and thermal expansion properties computed according to reference [1]. In addition to stiffness and thermal expansion properties, the fracture simulations require four additional input properties. These properties are the strength and fracture toughness of the matrix material and of the fiber/matrix interface. The matrix strength and fracture toughness are 77 MPa and 177 J/m<sup>2</sup>, respectively. The interface of this material system is chemically optimized and is thus quite strong. Without specific data on the correct interfacial values, we set the interfacial strength and fracture toughness equal to those of the matrix material. We do not allow the fibers to fracture. As a reference, the experimentally-determined composite strength and Mode I fracture toughness values to which we will be comparing are 66 MPa and 225 J/m<sup>2</sup>, respectively.

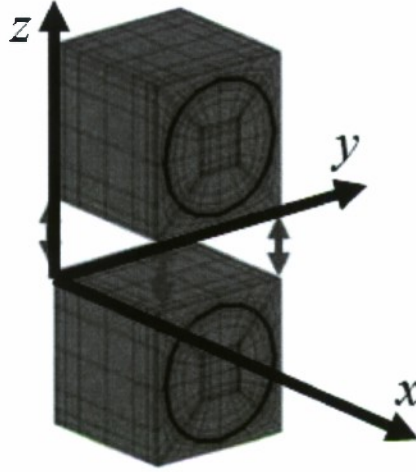


Figure 6. Cubic unit cell fracture model.

Table 2. Constituent properties for IM7/5240-4 cubic cell composite

	IM7 Fiber	5250-4 Matrix	Composite
$E_{xx}$ (GPa)	276	3.45	167
$E_{yy}, E_{zz}$ (GPa)	27.6		11.0
$\nu_{xy}, \nu_{xz}$	0.300	0.350	0.320
$\nu_{yz}$	0.800		0.510
$G_{xy}, G_{xz}$ (GPa)	138	1.28	5.33
$G_{yz}$ (GPa)	7.67		2.72
$\alpha_{xx}$ ( $^{\circ}\text{C}$ )	$-0.0360 \times 10^{-6}$		$0.372 \times 10^{-6}$
$\alpha_{yy}, \alpha_{zz}$ ( $^{\circ}\text{C}$ )	$5.04 \times 10^{-6}$	$46.8 \times 10^{-6}$	$24.3 \times 10^{-6}$

To calculate the Mode I fracture toughness for the unidirectional composite, periodic boundary conditions are applied on the  $x=\{0, L\}$  and  $y=\{0, L\}$  surfaces. The  $z$ -displacement is constrained on the  $z=-L$  surface, and the  $z$ -displacement is incrementally prescribed on the  $z=L$  surface. Denote the applied displacement  $u_z$  and consider a function  $T(\Delta u)$  defined parametrically with a parameter  $u_z$  as follows:

$$T(\Delta u) = \begin{cases} T = \langle \sigma \rangle_{zz}(u_z) \\ \Delta u = u_z - H[(C^{-1} \langle \sigma \rangle)_z + \varepsilon_{thermal}] \end{cases} \quad (22)$$

where  $\langle \sigma \rangle_{zz}$  is the  $zz$ -direction volume average stress in the unit cell,  $H$  is the height of the unit cell ( $2L$  in the cubic case), and  $\varepsilon_{thermal}$  is the residual strain due to curing. The displacement gap ( $\Delta u$ ) is the difference between the total displacement and the displacement due to linear elastic mechanics, i.e., the displacement gap is the

displacement due to fracture of the composite. It is clear from equation (22) that the composite stiffness and thermal parameters must be known *a priori* to calculate the displacement gap. The unidirectional properties are computed according to [1], and thus the effective stiffness matrix ( $C^E$ ) components can be determined from the auxiliary problems for the RVE according to the formula

$$C_{ijkl}^E = \frac{1}{|Q|} \int_Q \{ C_{ijmn}(y) \left( (e(w^{kt}))_{mn} + \bar{e}_{mn}^{ij} \right) \} dy, \quad (23)$$

where  $Q$  represents the unit cell, and the  $w$  functions are  $Q$ -periodic solutions to the basis unit strains  $\bar{e}^{ij}$  solving the six equations

$$\text{div}\{C(y)(e(w^{ij}) + \bar{e}^{ij})\} = 0. \quad (24)$$

Additionally, the effective composite thermal expansion coefficients can be determined by an additional computation using the six basis solutions  $w^{ij}$ , namely

$$H_{ij}^E = \frac{1}{|Q|} \int_Q \{ C_{mnop}(y) \left( (e(w^{ij}))_{op} + e_{op}^{ij} \right) : e_{mn}(y) \} dy. \quad (25)$$

In this case the auxiliary RVE problem is

$$\text{div}\{C(y)[e(\eta) - e(y)]\} = 0, \quad (26)$$

where  $e(y)$  is the inelastic strain due to the mismatch of constituent thermal expansion coefficients. Here,  $\eta$  is  $Q$ -periodic and  $e(\eta)$  gives the thermal strains. Figure 7 illustrates the results of the cubic cell model fracture simulation. The strength of the composite is predicted by the maximum of the volume average stress value or  $\max_{\Delta u \in \mathbb{R}} \{T(\Delta u)\}$ . The fracture toughness of the composite is calculated by integrating the volume average stress over the real number line with respect to the displacement gap (the area under the curve in Figure 7), or

$$G_{Ic} = \int_{\mathbb{R}} T(\Delta u) d(\Delta u) \quad (27)$$

The predicted composite strength for the cubic model is 77 MPa, and the predicted fracture toughness is 177 J/m<sup>2</sup>. The experimentally determined composite strength and fracture toughness values are 66 MPa and 225 J/m<sup>2</sup>, respectively. Simulations were performed at both the stress-free temperature and room temperature, with no difference being realized by including the thermal prestress in the computation. The  $\Delta T$  for the room temperature simulations was -150°C. The result of this model yielded no ability to predict realistic strength and fracture toughness of the composite.

We concluded a more realistic microstructure and crack path is necessary to move this solution toward the experimental values.

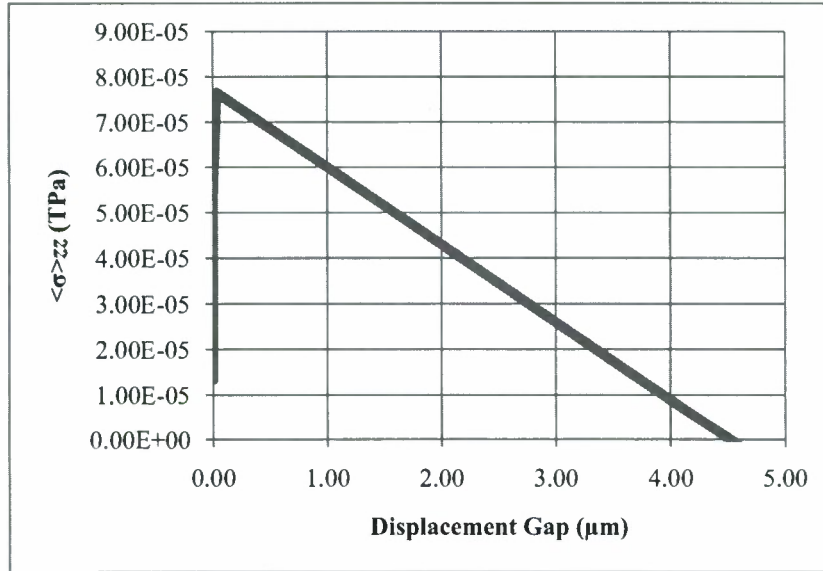


Figure 7. Traction-displacement gap plot for cubic unit cell.

### b. Hexagonal Unit Cell

After the cubic unit cell failed to produce realistic strength and fracture toughness predictions, a slightly more complicated two-fiber (total) hexagonally packed cell model was employed. The dimensions of this rectangular prism cell were  $L\sqrt{3} \times L\sqrt{3} \times L$  ( $x \times y \times z$ ), with the origin of the coordinate system shown in Figure 8. The location of the cohesive zone (fracture surface for this model) is again indicated by the red arrows. As in the cubic model, periodic boundary conditions were applied on the  $x = \{0, L\sqrt{3}\}$  and  $y = \{0, L\sqrt{3}\}$  surfaces, while the  $z$ -displacement was constrained on the  $z = 0$  surface, and the  $z$ -displacement was incrementally prescribed on the  $z = L$  surface. The input properties for the fiber, matrix, and fiber/matrix interface domains were identical to those used in the cubic unit cell section (see Table 2), however the ply level stiffness and thermal expansion properties varied slightly from the cubic model (see Table 3). These differences are a result of the different fiber microstructure and are not a reflection upon the resolution of the simulation. The traction-displacement gap simulation results for the hexagonal RVE are given in Figure 9. Simulations were performed at the stress-free temperature and at room temperature, with no difference in the prediction realized by including the thermal prestress. The composite strength and mode-I fracture toughness predicted by this model are 91.8 MPa and 222 J/m<sup>2</sup>, respectively. In this case the predicted mode-I fracture toughness is actually within 2% of the experimental value, 225 J/m<sup>2</sup>. However, the predicted composite strength moved in the wrong direction and is now 39% higher than the experimental value, 66 MPa.

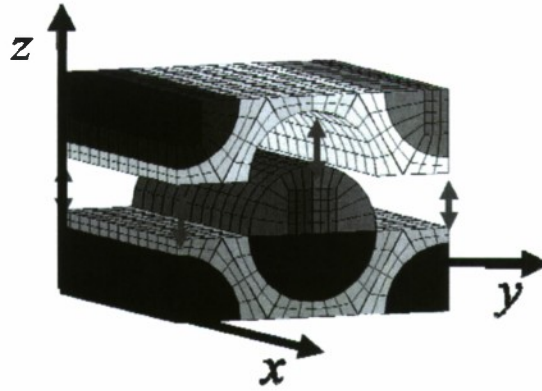


Figure 8. Hexagonal unit cell fracture model.

Table 3. Ply level properties for the IM7/5250-4 hexagonal cell composite

	Composite
$E_{xx}$ (GPa)	167
$E_{yy}, E_{zz}$ (GPa)	9.70
$\nu_{xy}, \nu_{xz}$	0.317
$\nu_{yz}$	0.557
$G_{xy}, G_{xz}$ (GPa)	4.97
$G_{yz}$ (GPa)	3.12
$\alpha_{xx}$ ( $^{\circ}\text{C}$ )	$0.369 \times 10^{-6}$
$\alpha_{yy}, \alpha_{zz}$ ( $^{\circ}\text{C}$ )	$24.8 \times 10^{-6}$

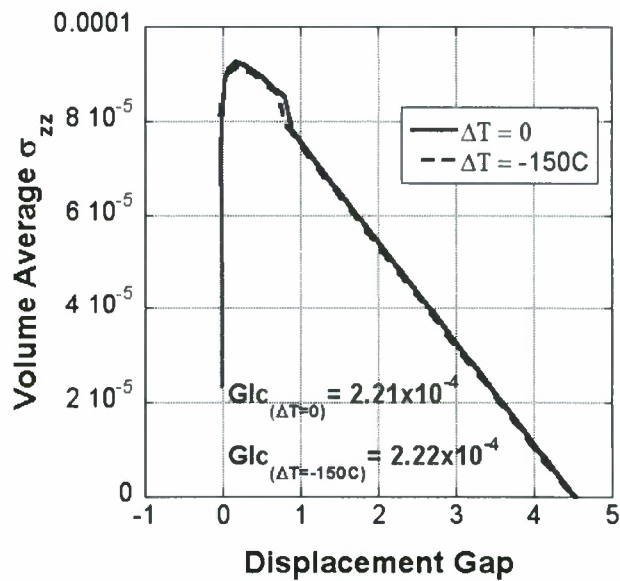


Figure 9. Traction-displacement gap plot for hexagonal unit cell.

Encouraged by the fracture toughness result on the hexagonal cell, we observed that our fracture surface was not particularly realistic for such a fiber microstructure and could thus be adversely affecting our predicted strength value. We investigated strength and fracture toughness according to the total crack length. The influence of the intra-phase or matrix crack path on the predicted values of the strength and fracture toughness was investigated next. The fiber packing, material, and interfacial properties are identical to the previous hexagonal cell model. The configuration of the fracture surface is shown in Figure 10. Here, cohesive zone interfaces are included on all fiber/matrix interfaces, Figure 10.a, and two mesh independent cracks (MICs – previously described) are used to connect the interfacial cohesive zones (see Figure 10.b) to create a contiguous composite fracture surface.

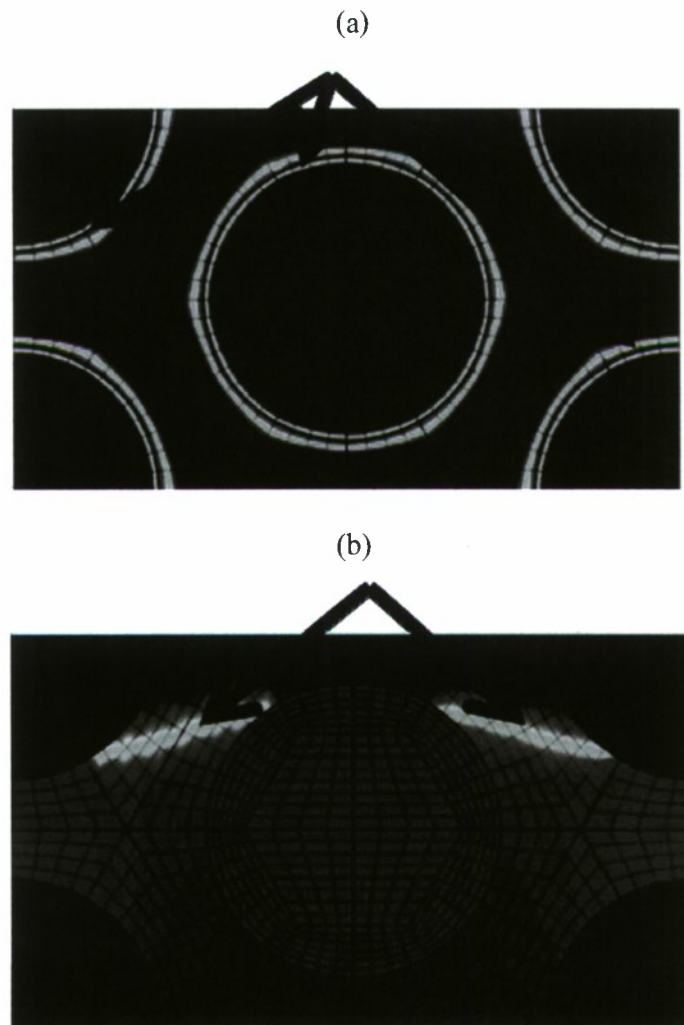


Figure 10. Configuration of the fracture surface in the hexagonal unit cell.

The location of the MICs connecting the interfacial cohesive zones was varied to change the crack length. Figure 11 shows a schematic of the different MICs and includes their relative crack lengths. Only the top half of the hexagonally packed cell is included

in this schematic. The angles that are used to describe the MICs are measured from the horizontal through the center point of the central fiber. For, example, the 60° MIC originates at the central fiber fiber/matrix interface at a 60° angle measured from the horizontal of the central fiber and terminates at the upper right fiber fiber/matrix interface at a 240° measured from the horizontal of the center of the upper right fiber. A symmetric MIC was used to connect the central fiber interfacial cohesive zone to the upper left fiber interfacial cohesive zone. The 65° crack is essentially the crack that is tangent to both fibers and thus produces the shortest overall crack length.

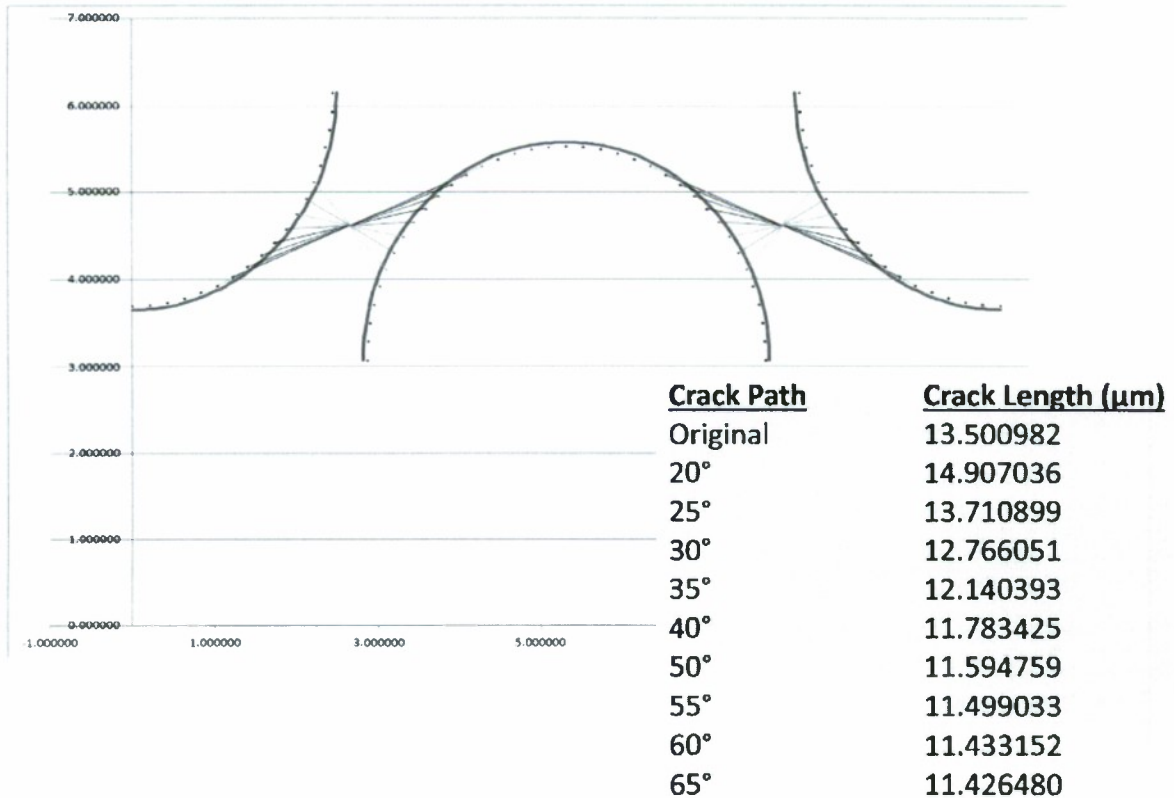


Figure 11. Schematic of mesh independent cracks connecting interfacial cohesive zones.

The traction-displacement gap results of the MIC fracture simulations for various crack path angles are shown in Figure 12. It is clear that both composite strength and composite fracture toughness are affected by crack length/crack path. Note that the 20° and 25° crack paths are longer than the original crack path and have larger strength and fracture toughness, while all crack paths shorter than the original predict decreased strength and fracture toughness. In general, strength and fracture toughness appear to be linearly related to the crack length for this microgeometry and the set of MIC definitions. Minimizing the crack length decreased the predicted composite strength from 91.8 MPa (original crack) to 75.2 MPa (65° crack), which is now only 14% too large. While this is a massive improvement over the original 39% error, this result is not satisfactory. The main problem is that by minimizing the crack length, the fracture toughness prediction

also decreased and now has a 20% error. These concerns will be addressed in the Future Directions section and are attributed to the necessity of looking at more complex RVE.

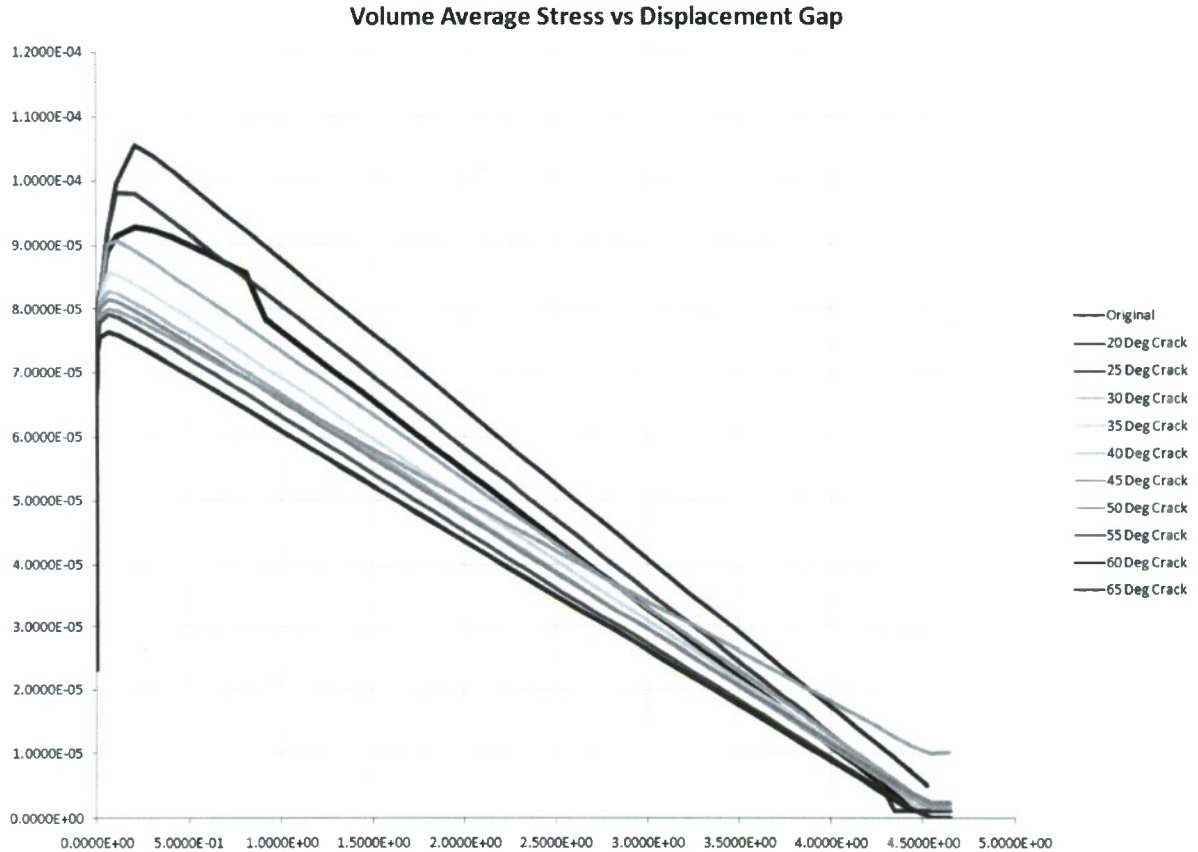


Figure 12. Traction-displacement gap plot for crack path experiment.

### c. Application to Thermal Oxidation

Although further work is needed to improve and validate the homogenization of the fracture toughness and strength based on RVE fracture simulation, a strong need for such methodology prompted an early application of the proposed technique. This section applies the computational machinery discussed above to a thermal oxidation problem for the AFRL/RXBC Hybrid Materials for Extreme Environments Program. An in-depth discussion of the harsh service environments of high-temperature composite materials is beyond the scope of this report, however, references [27-28] describe some recent micro-mechanical work that has been performed relative to these environments and will provide a good background. The main issue is that at high temperatures, the resin system will oxidize, altering the mechanical properties of the composite. From a mechanics standpoint the oxidized resin becomes slightly stiffer and most importantly significantly shrinks. This shrinkage causes effective shrinkage of the composite and creates significant stresses. These stresses, in turn, lead to crack initiation, which provides

additional pathways for oxidation, etc. To evaluate the cracking stresses and simulate the crack propagation on the ply level effective composite properties, both Group I and Group II properties are required. In the case of traditional composites, as was discussed in the comments pertaining to properties in Table 2, they can be measured directly. A completely different situation is encountered in the problem at hand. Obtaining a uniformly oxidized state in a sufficiently large composite *sample without significant amount of cracking* is not possible. Only the neat resin sample can be tested in this condition. Thus application of multi-scale analysis may be the only approach to solving coupled thermal oxidation cracking problems in composite and hybrid materials. In the present section only effective property predictions will be addressed. Both Group I and II effective properties for G3-500/PMR15 composite material system in both the oxidized and nonoxidized regions were computed as discussed below. The hexagonal fiber packing geometry was used, with a fiber diameter of 7 $\mu$ m and a fiber volume fraction of 51%. The 65° (tangent) crack path is used for the MICs. The nonoxidized and oxidized properties of the G3-500 fiber, PMR15 resin, and resulting composites are listed in Table 4. The fiber and resin properties were given as inputs, and all composite properties were calculated according to reference [1].

Table 4. Nonoxidized and oxidized properties of the G3-500 fiber, PMR15 resin, and composite

	<b>G3-500 Fiber</b>	<b>Non Oxidized PMR15 Resin</b>	<b>Non Oxidized Composite</b>	<b>Oxidized PMR15 Resin</b>	<b>Oxidized Composite</b>
<b>E<sub>xx</sub> (GPa)</b>	237	3.39	123	4.09	123
<b>E<sub>yy</sub>, E<sub>zz</sub> (GPa)</b>	23.7		7.64		8.79
<b>v<sub>xy</sub>, v<sub>xz</sub></b>	0.300	0.330	0.313	0.330	0.313
<b>v<sub>yz</sub></b>	0.800		0.523		0.536
<b>G<sub>xy</sub>, G<sub>xz</sub> (GPa)</b>	119	1.27	3.81	1.54	4.59
<b>G<sub>yz</sub> (GPa)</b>	6.59		2.50		2.86
<b>Axial (xx) Shrinkage (/h)</b>	0.00	$7.6 \times 10^{-6} \times t$	$1.06 \times 10^{-7} \times t$	$2.20 \times 10^{-3} + 7.6 \times 10^{-6} \times t$	$3.68 \times 10^{-5} + 1.27 \times 10^{-7} \times t$
<b>Transverse (yz) Shrinkage(/h)</b>	0.00		$4.24 \times 10^{-6} \times t$		$1.23 \times 10^{-3} + 4.24 \times 10^{-6} \times t$

The fracture simulation was carried out for both the nonoxidized and oxidized composite materials at time values of 200, 600, and 1000 hours. The experimentally determined strength and G<sub>1c</sub> data for the nonoxidized/oxidized resin were 40/20 MPa and 500/250 J/m<sup>2</sup>, respectively. Table 5 reports the G3-500/PMR15 strength and Mode I fracture toughness predictions for the nonoxidized and oxidized composite. The “Non” refers to the nonoxidized composite, and the input fiber/matrix interfacial strength and fracture toughness are equal to the respective nonoxidized resin values presented above (40 MPa and 500 J/m<sup>2</sup>). “Ox1” refers to the oxidized composite in which the fiber/matrix interfacial strength and fracture toughness values are equal to the respective values of the oxidized resin (20 MPa and 250 J/m<sup>2</sup>). Finally, “Ox2” refers to the oxidized composite in

which the fiber/matrix interfacial strength and fracture toughness values are equal to ¼ the oxidized resin values (5 MPa and 62.5 J/m<sup>2</sup>).

Table 5. G3-500/PMR15 transverse strength and G<sub>Ic</sub> predictions

	<b>Non, 200h</b>	<b>Non, 600h</b>	<b>Non, 1000h</b>	<b>Ox1, 200h</b>	<b>Ox1, 600h</b>	<b>Ox1, 1000h</b>	<b>Ox2, 200h</b>	<b>Ox2, 600h</b>	<b>Ox2, 1000h</b>
<b>Strength (MPa)</b>	42.4	42.4	42.3	21.2	21.1	20.9	11.8	11.7	11.6
<b>G<sub>Ic</sub> (J/m<sup>2</sup>)</b>	559	556	557	279	278	277	153	153	152

The Ox2 simulation was used to test sensitivity to the fiber/matrix interfacial strength and fracture toughness parameters. In the real composite, the degradation of the interfacial properties due to oxidation is at this time unclear at best. These property predictions were passed to a laminate-level analysis to predict crack growth and oxidation layer growth within the laminate. The laminate-level analysis is beyond the scope of this report. This multi-scale materials problem, however, represents a scenario which will occur with increasing frequency in the years to come with emerging material systems. Namely, some basic information about the constituent materials will be available, but little or no composite-level data will be available. Computational materials science will deliver predictive guidance on how to tailor the microstructure select materials to enable the revolutionary concept of “the right material in the right spot for optimized performance.”

#### **d. Future Directions**

We showed that the microstructure and crack path play large roles in the strength and fracture toughness predictions. Indeed, we found that in the hexagonal RVE, i.e. in a uniformly distributed hexagonal fiber array, the crack path was seemingly not short enough to reach the experimentally-determined strength, and the crack path was not long enough to maintain the fracture toughness near the experimental value. This situation appears to be a dichotomy, except that other factors in the microstructure can and do affect the strength and fracture toughness of the composite. Consider, for instance a randomly distributed array of 20 fibers, one realization of which is shown in Figure 13. Note the irregularity of the fiber spacing. The proximity of fibers to each other causes increased stress concentrations in the matrix domain that will begin to fracture the composite at much lower load states than the regularly-spaced cubic and hexagonal models presented above. Initiating cracks at lower load steps will decrease the strength prediction for a given simulation. As for the fracture toughness, it is easy to see from Figure 13 that the crack path will be more torturous than the tangent crack path in the hexagonal cell, and thus the crack length will, in general, be longer. Decreasing the strength while maintaining the crack length should produce predictions that more closely match the experimental values. In order to use a random fiber packing, one must first verify that the realization of the microstructure produces ply-level stiffness properties consistent with experimental values. It is expected that, for a small numbers of fibers, the

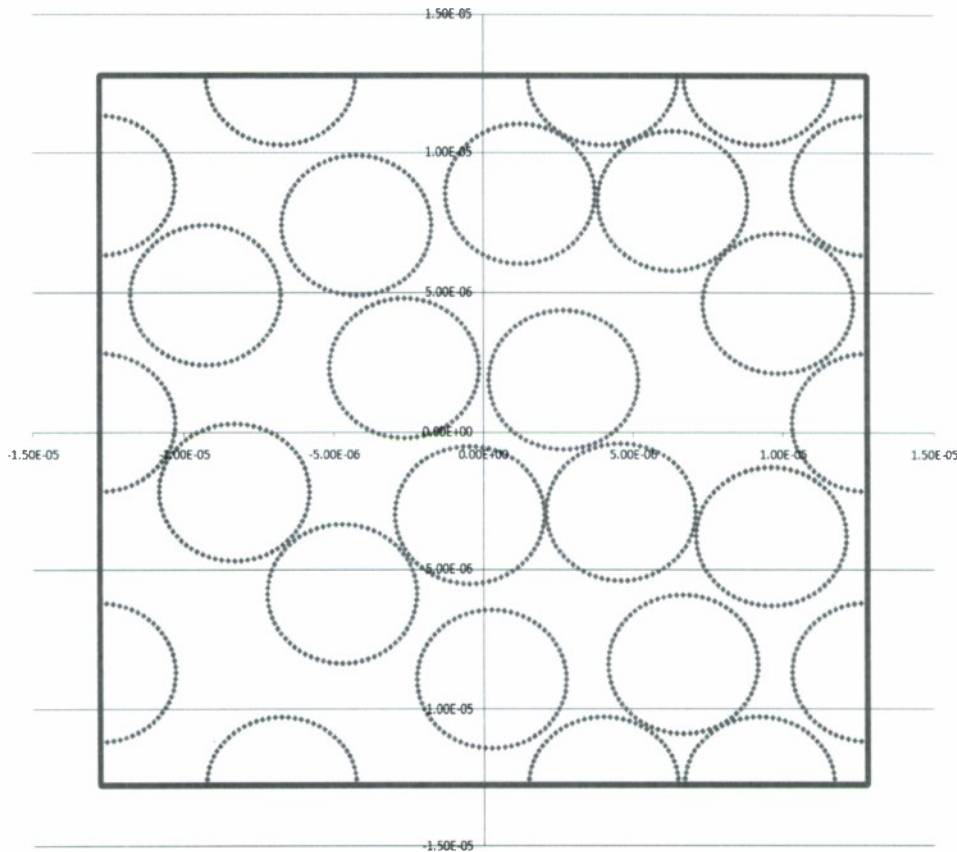


Figure 13. Schematic of 20 randomly distributed fibers.

mechanical properties will vary greatly with the realization. This dependence should decrease as the number of fibers in the model increases. Very limited work has been done on investigation of random fiber packing and RVE sizes on effective stiffness properties [6, 29], and the effective fracture property prediction is not addressed at all at present.

Another consideration to be taken into account is of a more fundamental nature. It concerns the physics of small scale cracking. Neither the classical Griffith fracture mechanics nor the cohesive zone model used above are explicitly capturing length scale specific effects, e.g. surface tension, which may become important at the sub-micro and nano length scale [30]. It is thought that the future development path of SCSAM framework should include such nonclassical crack models at a small length scale.

Prior to returning to the ply level simulations in the next section, we would like to return to the material property in Table 1 and discuss additional developments needed to address the Group II properties not considered above, namely shear deformation related strength and Mode II fracture toughness. The framework for homogenization of these characteristics is similar to Eqn. ( 22); what is different is the cracking pattern which occurs in the RVE. The fracture surface is expected to be significantly more complex. Additional development of MIC framework is required to simulate such fracture phenomena.

## 5. Complex Interactive Cracking Network Simulation on the Ply Level

In this section we demonstrate the capability to model complex failure phenomena based on the MIC and interface delamination framework on the ply level. As outlined in the previous section, some of the properties required for the ply level analysis cannot be obtained by means of homogenization at present. It is, however, one of the critical practical advantages of SCSAM that the analysis development at various scale levels can progress independently and at all stages evaluated against experimental data.

Consider a multilayered composite plate consisting of  $N$  orthotropic layers with in-plane dimensions  $L$  and  $W$  in the  $x$ - and  $y$ -directions, respectively. Let the thickness of the plate be  $H$  ( $z$ -direction) as shown in Figure 14. Each ply represents an orthotropic material which is characterized by engineering stiffness constants  $E_{ij}$ ,  $G_{ij}$ ,  $\nu_{ij}$  and thermal expansion coefficients  $\alpha_{ij}$  ( $i,j=1,2,3$ ). The direction  $x_1$  coincides with the direction of the fiber and the angle  $\theta$  between the direction of the global coordinate  $x$  and the fiber direction  $x_1$  in a given ply is called the ply orientation.

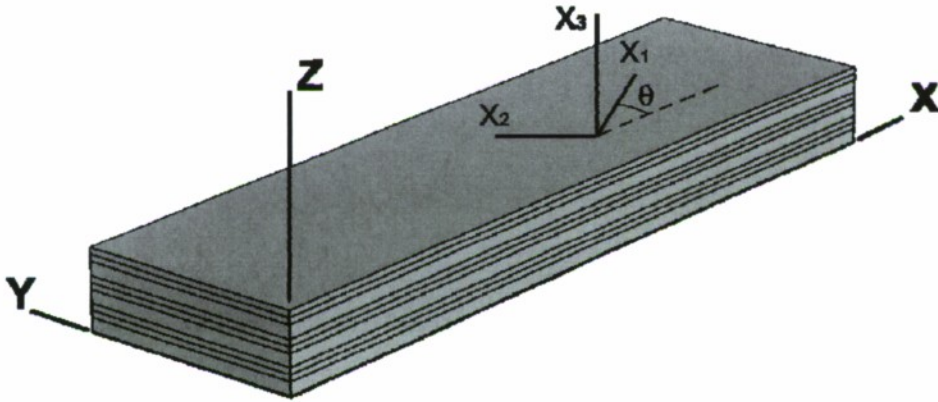


Figure 14. Multilayered composite plate and the coordinate system.

Tensile loading in the  $x$ -direction will be applied by incrementing the displacement  $u_x$  at the edges  $x=0, L$  so that

$$u_x^i(0,y,z) = u_x^{i-1}(0,y,z) - \Delta^i \quad \text{and} \quad u_x^i(L,y,z) = u_x^{i-1}(L,y,z) + \Delta^i \quad (28)$$

where  $\Delta^i$  is a constant and  $i$ -is the number of the loading step. Such incremental formulation is required to properly account for the thermal curing stresses prior to mechanical loading. The displacement field  $u_x^0$  appearing in equation (2) is computed by

solving a thermal mechanical expansion problem under boundary conditions, which simulate free expansion and only restrict rigid body motion, i.e.

$$u_x^0(0,0,0)=0, u_y^0(W,0,0)=0 \text{ and } u_z^0(x,y,z)=0. \quad (29)$$

The incremental loading boundary conditions ( 28) are supplemented with constraint conditions on the other displacement components at the lateral edges  $x=0$  and  $L$ , so that

$$u_y^i(0,y,z)=u_y^0(0,y,z) \text{ and } u_z^i(L,y,z)=u_z^0(L,y,z), \quad (30)$$

which means that all displacement components except axial are fixed at the edges. The analysis begins from an initially undamaged state (Figure 15.a). As a result of load application, matrix cracks will form in each ply of the laminate as shown in Figure 15.b. Their location is arbitrary and not predetermined before the analysis. At some value of the applied load, the delaminations between plies will appear as a result of matrix cracking, as shown in Figure 15.c, and cause disintegration of the composite laminate. Note that some of the plies may have fiber orientation  $\theta=0$  coinciding with the loading direction, in which case these plies will continue to carry load after complete delamination of the specimen. The fiber failure mode will not be treated in the present manuscript and is deferred to further work.

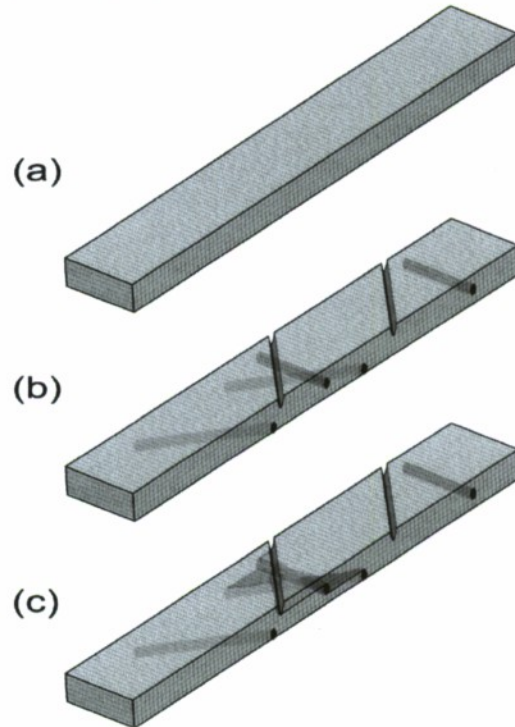


Figure 15. Damage progression sequence in a laminated composite plate subjected to tensile loading. (a) initial stage without damage, (b) matrix cracking stage, (c) delamination stage, linking up matrix cracks in various plies.

The initial stress fields (prior to crack initiation) in the flat laminates under axial tension conditions are highly uniform in the x-direction, and therefore the initial crack insertion locations have a tendency to cluster depending on the last digit of computer number representation. To obtain more realistic initial crack insertion patterns and mimic inevitable statistical variability, quasi-random strength properties were generated across the coupon volume. Distributions of random transverse strength properties  $y_t$  (tensile),  $y_c$  (compressive) and  $s$  (shear strength) were assumed to follow classical two-parameter Weibull law defined as

$$P(x) = 1 - \exp\left\{-\frac{v}{V_0}\left(\frac{x}{A_x}\right)^{\beta_x}\right\}; \quad x = y_t, y_c, s \quad (31)$$

where  $A_x$  and  $\beta_x$  are scale and shape parameters of corresponding strength properties. The same value of  $\beta = 12$  was assumed for all strength distributions, based on transverse tensile strength scaling in carbon epoxy composites. Using average strength values  $X$ , shown in Table 1 for the IM7/8552 composite, given in Ref. [32], scale parameters were calculated as

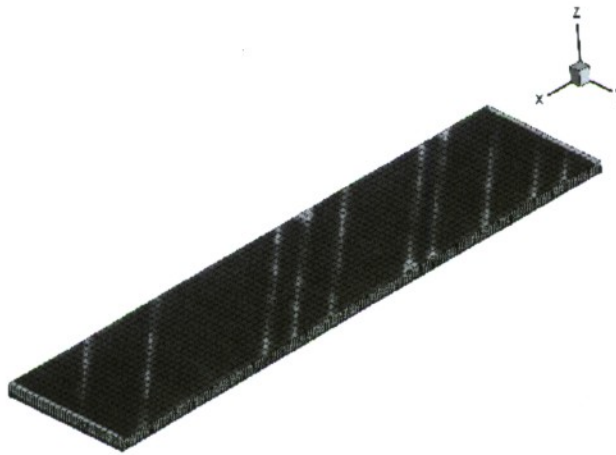
$$A_x = X / \Gamma(1 + 1/\beta_x); \quad X = Y_t, Y_c, S$$

To ensure mesh independence of generated quasi-random strength characteristics [31], they were normalized by the reference volume  $V_0 = 6250 \text{mm}^3$  (typical of an 8-ply unidirectional composite, which is used for transverse strength measurement) and corresponding local volumes  $v_i$ . Since failure criterion was applied in individual integration points, a “local volume”  $v_i$  was associated with each integration point as a product of the Gauss weight and Jacobian so that  $\sum_{i=1}^{INP} v_i = V_n$ , where  $INP$  is the total number of integration points and  $V_n$  is the volume of the n-th ply. Note that the random distribution of initial strength (31) was only utilized for crack origination purposes. There was no variability introduced in the decohesive law. This simplified definition requires modifications for systematic studies of stochastic strength distribution effects on the apparent strength of composites and is used below only for method demonstration purposes.

The methodology presented above was applied to perform the fracture analysis of the same quasi-isotropic laminate as considered in [32] and in the section above but without any predefined matrix cracking patterns. The analysis methodology correctly predicted both the sequence of the delamination, the failure loads and the multistep load drop behavior before the final failure that was experimentally observed in [32]. The load carried after the delamination process corresponds to the load carried by the 0 plies until fiber failure. Figure 16 displays the z-direction displacement map during the stochastic crack insertion simulation for three simulation load steps. The first two load steps (305 MPa and 406 MPa) show accumulation of the matrix cracking and delamination onset at the free edge and matrix crack pockets. The third load step (495 MPa) immediately precedes the full delamination of the -45/0 interface and the associated load drop.



a)



b)



c)

Figure 16. Vertical (z-direction) displacement map at the different load steps: (a) 305 MPa; (b) 406 MPa; (c) 495 MPa.

## Appendix: Composite Scarf Repair Optimization for the JSF

This appendix contains a final summary of the composite scarf repair optimization that was chiefly performed during the previous grant period. Final experimental data and optimized strength predictions were not available at the time of the previous final report and are included here. For a comprehensive description of the work, please refer to reference [33], which also includes numerical results concerning patch-cure warpage, overply thickness, and overply fiber orientation angle which are not presented here.

The scarf repair is used to restore strength to a composite material after it has been damaged. The repair process removes the damaged material and fills the void with an inverted, truncated, conical patch which is adhesively bonded to the remaining original material (see Figure A1). The current standard repair involves at least one double overlay ply (overply) to restore the maximum amount of strength. In Figure A1, the green area represents the original material, the yellow is the adhesive, the red is the scarf repair patch, and the blue is the overply.



Figure A1. Composite scarf repair models (with and without the overply).

One problem with the current scarf repair system is the necessary inclusion of the overply to restore strength. It is clearly seen in Figure A1 that the overply adds thickness to the original material and changes the outer mold line. This situation adversely affects the stealth properties of the structure, as well as increases the weight and size of the repair. One goal of this work is to improve the strength of the repair without the overply to alleviate the negative impacts the overply has on the other critical properties of the structure.

It was previously found [33] that the nonlinear adhesive modeling/failure is a critical factor in composite scarf repair strength prediction. The nonlinear elastic constitutive equations for the adhesive material consider only variation of the Young's moduli and assume constant Poisson's ratio in accordance with the experimental observations. The shear modulus  $G$  is expressed as

$$G = \min \left[ \frac{E_1(J_1)}{2(1+\nu)}, G_2(J_2) \right], \quad (A1)$$

where the elastic modulus,  $E_1$ , is a monotonic function of strain calibrated using cubic spline interpolation from experimental tensile testing and is expressed through the dilatational strain invariant,  $J_1$ . Similarly,  $G_2$  is the shear modulus calibrated based on

KGR-1 experimental test results and is expressed through the distortional strain invariant  $J_2$ , where

$$J_1 = \varepsilon_1 + \varepsilon_2 + \varepsilon_3, \quad (A2)$$

$$J_2 = \sqrt{\frac{1}{2}((\varepsilon_1 - \varepsilon_2)^2 + (\varepsilon_3 - \varepsilon_2)^2 + (\varepsilon_1 - \varepsilon_3)^2)},$$

and  $\varepsilon_i$  are the principle values of strain. Equation (A1) is also used to predict the failure of the adhesive. Critical values of the strain invariants ( $J_1$  and  $J_2$ ) are backed out via simulation using the experimental testing on the neat adhesive. After strain values result in invariants exceeding one of these critical values, the shear modulus is set to a small positive value. Reference repair strength test values were reproduced by using such adhesive constitutive modeling with accuracy.

The time of such nonlinear solution was still unfeasible for optimization studies. Instead, the chosen goal function minimizes the elastic  $L^p$  norm of the deviatoric stress invariant in the adhesive regime. This approach determines optimal repair fiber orientations in a cost-efficient manner. For strength prediction purposes, a fully nonlinear analysis is performed for the optimized layout.

Scarfig, repair, and testing of the specimens were performed in the Materials & Manufacturing Systems Support Division (RXSA). Normalized experimental strength data are presented in Figure A2. The virgin material strength reference is for the ASTM standard 25.4 cm  $\times$  2.54 cm coupons. All other tests used the large 57 cm  $\times$  13 cm coupon size. The virgin material is used only as a reference data set to determine material properties and calibrate the critical failure volume parameters [34]. Strength prediction values closely match the experimental values in Figure A2. The results in Figure A2 confirm that the optimization increases the strength of the repair. Note that the orange bar is the standard repair *with* an overply, and the red bar is the optimized repair *without* an overply. The optimized repair without an overply is 10% stronger than the standard repair with an overply. Additionally, the repair is 20% lighter, 10% smaller, and is flush with the original material surface and thus does not affect the mold line (stealth properties) of the structure.

As a result of the success of this work, the JSF Repair Group (headed at NAVAIR) is testing our optimized repair layouts for use on the JSF structure. One challenge the JSF repair faces is how the adhesive behaves in hot and wet environments. As the temperature increases and the environment moistens, the adhesive becomes much more compliant and thus fails at smaller loads. Since this optimization methodology results in a repair that minimizes the adhesive stress, it is a natural fit for such an environment. The results of the JSF testing are currently not available.

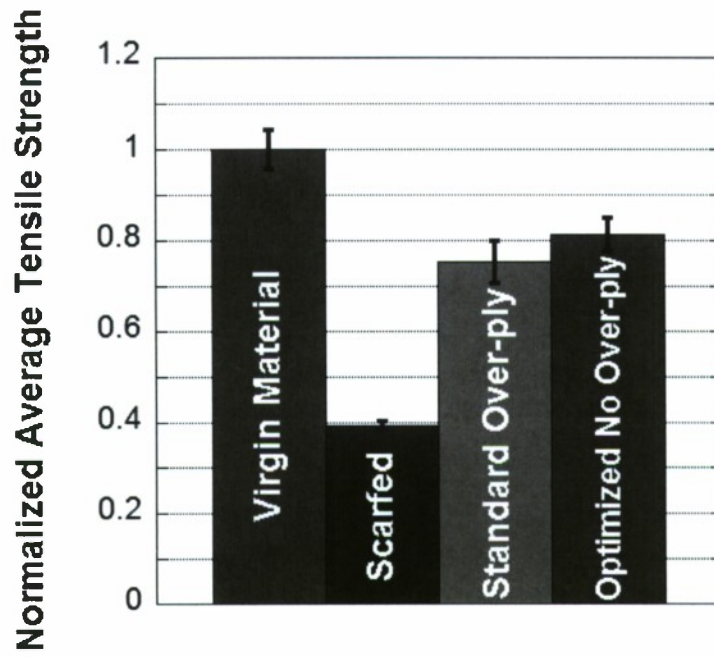


Figure A2. Normalized experimental repair strength.

## References

1. Breitzman, T., Lipton, R. and Iarve, E.V. (2007), Strength assessment and local field extraction in multi-scale materials, *Journal of Multiscale Modeling and Simulation*, **6**, pp. 937-962
2. Lipton, R. (2003), Assessment of the local stress state through macroscopic variables, *Philosophical Transactions of the Royal Society of London A*, **361**, pp. 921-946.
3. Lipton, R. (2004), Bounds on the distribution of the extreme values for the stress in composite materials, *JMPS*, **52**, pp.1053-1069.
4. Chaboche, T. L., O. Lesne, T. Pottier. (1998), Continuum damage mechanics of composites: towards a unified approach, In: G.Z. Voyiadjis, J.W. Ju, J.L Chaboche (Eds.), *Damage Mechanics in Engineering Materials*, Elsevier Science Ltd, Oxford, UK, pp. 3-26.
5. Talreja, R. (1989), Damage development in composite: mechanism and modeling, *J. Strain Analysis*, **24**, pp. 215-222.
6. Swaminathan, S., S. Ghosh. (2006), Statistical equivalent representative volume elements for unidirectional composite microstructures: Part II – with interfacial debonding, *Journal of Composite Materials*, **40**(7) pp. 605-622.
7. Iarve, E.V., Mollenhauer, D. and Kim, R. (2005), Theoretical and experimental investigation of stress redistribution in open hole composite laminates due to damage accumulation, *Composite: Part A* , **36**, pp. 163-171.
8. Wawrzynek, P.A., Ingraffea, A.R. (1989), An interactive approach to local remeshing around a crack tip, *Finite Elements in Analysis and Design*, **5**(1) pp 87-96.
9. Fish, J. and Markolefas, S. (1992), The s-method of the finite element method for multilayered laminates, *Int. J. Num. Meth. Eng.*, **33**, pp 1081-1105.
10. Iarve, E. V. (1997), Three-dimensional stress analysis in open hole composite laminates containing matrix cracks, *AIAA-98-1942*.
11. Moes, N., Dolbow, J., Belytschko, T. (1999), A finite element method for crack growth without remeshing, *Int. J. Num. Meth. Eng.*, **46**, pp 601-620.
12. Belytschko, T., Parimi, C., Moes, N., Sukumar, N., Usui, S. (2003), Structured extended finite element methods for solids defined by implicit boundaries, *Int. J. Numer. Meth. Engng*; **56**:609–635.

13. Huynh, D.B.P., Belytschko, T. (2009), The extended finite element method for fracture in composite materials, *Int. J. Numer. Meth. Engng*; 77, pp 214-239.
14. Iarve, E. V. (2003), Mesh independent modeling of cracks by using higher order shape functions, *Int. J. Num. Meth. Eng.*, 56, pp 869-882.
15. Whitney, J. M. (1987), Structural analysis of laminated anisotropic plates, Technomic Publishing, p 339.
16. Turon, A., Camanho, P. P., Costa, J., Dávila, C. G. (2006), A damage model for the simulation of delamination in advanced composites under variable-mode loading, *Mechanics of Materials*, 38, pp 1072-1089.
17. Alfano, G., Crisfield, M. A. (2001), Finite element interface models for the delamination analysis of laminated composites: mechanical and computational issues, *Int. J. Num. Meth. Eng.*, 50, pp. 1701-1736.
18. Jiang, W-G., Hallett, S. R., Green, B. G., Wisnom, M. R. (2007), A concise interface constitutive law for analysis of delamination and splitting in composite materials and its application to scaled notched tensile specimens, *Int. J. Numer. Meth. Engng.*, 69, pp. 1982-1995.
19. Dávila, C. G., Camanho, P. P., Rose, C. A. (2005), Failure criteria for FRP laminates, *J. of Composite Materials*, 39(4), pp. 323-345.
20. König, M., Krüger, R., Kussamul, K., Gadke, M. (1977), Characterizing static and fatigue interlaminar fracture behavior of a first generation graphite/epoxy composite, ASTM STP 1242.
21. O'Brien, T. K. (1998), Composite interlaminar shear fracture toughness,  $G_{IIc}$ : shear measurement or sheer myth? *ASTM STP 1330*.
22. O'Brien, T. K. (1998), Interlaminar fracture toughness: the long and winding road to standardization, *Composites: Part B*, 29, pp. 57-62.
23. Bradley, W. L. (1989), Understanding the translation of near resin toughness into delamination toughness in composites, *Key Engineering Materials*, 17, pp. 61-198.
24. Tsotsis, T. K., Rugg, K. L., Cox, B. N. (2006), Towards rapid screening of new composite matrix resins, *Composite Science and Technology*, 66, pp 1651-1670.
25. Pagano, N. J., Schocppner, G., Abrams, F. (1998), Steady-state cracking and edge effects in thermo-mechanical transverse cracking of cross-ply laminates, *Composites Science and Technology*, Vol. 58, pp. 1811-1825.

26. Tandon, G. P., Pochiraju, K., Schoeppner, G. A. (2008), Thermo-oxidative behavior of high temperature PMR-15 resin and composites, *Materials Science and Engineering, Part-A*, Vol. 498, pp. 150-161.
27. Yu, Y., Pochiraju, K. (2008), Modeling long-term degradation due to moisture and oxygen in polymeric matrix composites, *Materials Science and Engineering, Part-A*, Vol. 498, pp. 162-165.
28. Pochiraju, K., Tandon, G. P. (2008), Evolution of stress and deformations in high-temperature polymer matrix composites during thermo-oxidative aging, *J. Mechanics of Time-Dependent Materials*, Vol. 12, pp. 45-68.
29. Swaminathan, S., Ghosh, S., Pagano, N. J. (2006), Statistical equivalent representative volume elements for unidirectional composite microstructures: Part II – without damage, *Journal of Composite Materials*, **40**(7) pp. 583-604.
30. Sendova, T., Walton, J. (2009), A new approach to the modeling and analysis of fracture through extension of continuum mechanics to the nanoscale, *Mathematics and Mechanics of Solids*.
31. Gurvich, M. R. (1999), *Comp. Sc. and Techn.*, **59**, N 11, pp 1701-1711.
32. Hallett, S. R., Jiang, W-G., Khan, B., Wisnom, M. R. (2008), Modeling the interaction between the matrix crack and delamination damage in scaled quasi-isotropic specimens, *Composites Science and Technology*, **68**,80–89.
33. Brcitzman, T., Iarve, E., Cook, B., Schoeppner, G., Lipton, R. (2009), Optimization of a composite scarf repair patch under tensile loading, *Composites Part A: Applied Science and Manufacturing*, **40**, pp. 1921-1930.
34. Iarve, E. V. , Mollenhauer, D. H., Whitney, T., Kim, R. (2006), Strength prediction in composites with stress concentrations: classical Weibull and critical failure volume methods with micromechanical considerations, *J. of Material Science*, **41**(20), pp 6610-6622.